



ELSEVIER

Surface Science 380 (1997) 245–257

surface science

X-ray reflectivity study on gold films during sputter deposition

R.P. Chiarello ^{a,*}, H. You ^a, H.K. Kim ^b, T. Roberts ^a, R.T. Kempwirth ^a, D. Miller ^a,
K.E. Gray ^a, K.G. Vandervoort ^a, N. Trivedi ^a, S.R. Phillpot ^a, Q.J. Zhang ^c, S. Williams ^c,
J.B. Ketterson ^c

^a Materials Science Division, Argonne National Laboratory, Argonne, IL 60439, USA

^b Department of Physics, Pusan National University, Pusan, South Korea

^c Department of Physics and Astronomy, Northwestern University, Evanston, IL 60208, USA

Received 16 November 1995; accepted for publication 18 November 1996

Abstract

We performed in-situ X-ray reflectivity measurements of gold films during sputter deposition on polished silicon substrates. The measurements were performed at several substrate temperatures and under two argon pressures. The gold surfaces were also examined by scanning tunneling microscopy after deposition to obtain their real-space topographic images. These images were used to complement the X-ray reflectivity measurements in determining the effect of argon pressure on the gold surface and its height–height difference functions. An approximation for height–height difference functions was employed to analyze the X-ray reflectivity data. The measured interface width during growth followed a simple power law, consistent with recent theoretical results of dynamic scaling behavior. The scaling exponents, however, do not agree well with predictions based on some models in 2 + 1 dimensions.
© 1997 Elsevier Science B.V.

Keywords: Atomic force microscopy; Gold; Growth; Metallic films; Metallic surfaces; Models of non-equilibrium phenomena; Non-equilibrium thermodynamics and statistical mechanics; Polycrystalline surfaces; Polycrystalline thin films; Scanning tunneling microscopy; Silicon; Solid–gas interfaces; Sputtering; Surface roughening; Surface structure, morphology, roughness, and topography; X-ray scattering, diffraction, and reflection

1. Introduction

The formation of rough interfaces plays an important role in fundamental processes currently of interest in many basic and applied scientific disciplines. Rough interfaces form in nature and in modern materials fabrication by the non-equilibrium dynamic exchange of material in processes such as corrosion, vapor-phase deposition, crystal

growth and dissolution, biological growth, and erosion of the earth's surface. Conventional methods of statistical mechanics and thermodynamics are not applicable to non-equilibrium processes. However, computer simulations have been used to determine that an evolving rough interface eventually reaches a steady state. This steady state can be described using principles of scale-invariance and fractal scaling [1].

The scaling behavior of several growth models has been studied in detail using analytical and computational methods (see Ref. [1], and references therein), but there have been a smaller number of experimental investigations of growing

* Corresponding author. Tel.: +1 415 723 5696;

Fax: +1 415 723 0495; e-mail: chiarello@stanford.edu

¹ Present address: Stanford University, 106 McCullough, Stanford, CA 94305, USA.

interfaces [2]. This can be attributed to the need for non-destructive in-situ measurements. X-ray reflectivity (XR) is a non-destructive microscopic probe suitable for in-situ investigations. Previous in-situ applications using XR include molecular beam epitaxy on semiconductor interfaces in ultra-high vacuum environments [7], electrochemical corrosion [8], and crystal growth and dissolution of minerals in contact with aqueous fluids [9].

In this paper, we investigated in situ the kinetic roughening of an interface formed by sputter deposition from a vapor phase under non-equilibrium conditions. Specular XR measurements were used to determine the thickness and root mean square (RMS) interfacial roughness (width) of gold vapor deposited onto silicon. Early results of this work were published elsewhere [10]. Gold was deposited onto clean, polished silicon by sputter deposition. The polished silicon provides a nearly ideal two-dimensional (2D) planar substrate, and sputter deposition was chosen because of its wide use in industrial deposition processes. Also, scanning tunneling microscopy (STM) was used for examination of the gold surface after deposition.

The aim of this work is two-fold: (i) to determine if the interfacial width exhibits dynamic scaling behavior during sputter deposition and, if so, to determine the exponents associated with the scaling behavior, and (ii) to investigate the effect of deposition conditions on the scaling exponents and on the nature of interfacial inhomogeneities both lateral to and normal to the substrate surface.

2. Background

2.1. Growth models and scaling behavior

A pivotal development in understanding kinetic roughening during growth resulted from a computational study of the Eden [11] and the ballistic aggregation [13] growth models by Family and Vicsek [12]. The central result was a postulation of scaling behavior

$$W(L, t) \approx L^\alpha f(t/L^{z/\beta}), \quad (1)$$

where $W(L, t)$ is the root mean square (RMS) width of the interface at time t , and L is the size of the lattice. The function $f(x)$ has the behavior,

$f(x) \approx x^\beta$ for $x \ll 1$, and $f(x) = \text{constant}$ for $x \gg 1$. The exponents α and z/β are the finite-size scaling exponent and the dynamic scaling exponent, respectively. Subsequent analytical and computational studies have centered on the determination of these exponents. Analytical studies have been performed using the Langevin equation. A simple linear Langevin equation has been studied by Edwards and Wilkinson [14]. Later, the lowest-order non-linear Langevin equation was studied by Kardar et al. [15]. The non-linear equation and more sophisticated forms of the linear Langevin equation were studied using solid-on-solid growth models [16,17].

The Langevin equation can be written as [18]

$$\frac{\partial h}{\partial t} = v \nabla^2 h - v_1 \nabla^4 h + \lambda (\nabla h)^2 + \lambda_1 \nabla^2 (\nabla h)^2 + \text{higher order terms} \dots + \eta(\mathbf{x}, t), \quad (2)$$

where $h(\mathbf{x}, t)$ is a function which gives the height of the surface from the original flat surface at time t and position \mathbf{x} . We assume that $h(\mathbf{x}, t)$ is a single valued function for our experimental conditions since the electron density of the sputter-deposited gold (as determined by XR) was nearly equal to that expected for bulk gold. The noise $\eta(\mathbf{x}, t)$ is Gaussian and is a function of the surface dimension d_s and t . For clarity we will denote $d = d_s + 1$ for the spatial dimension, \mathbf{r} for a vector in d dimensions and \mathbf{x} for a vector in d_s dimensions. The simplest case is when all v_s and λ_s are zero, which represents random growth. During random growth, an arriving atom sticks at the first site it hits and no diffusion of the atom is allowed. Then each point on the surface will be completely independent and the growth behavior follows Poisson statistics. That is

$$W = t^{1/2}. \quad (3)$$

The exponents are $\alpha = \text{undefined}$ and $\beta = 0.5$, independent of dimensionality. In the Edward and Wilkinson model [14], $v \neq 0$ and Fourier analyses have yielded the exact values of the exponents, namely, $\alpha = (3 - d)/2$ and $\eta = (3 - d)/4$. Specifically, for $d = 2 + 1$ dimensions, α and β are zero, and the RMS width shows a logarithmic divergence in time and in size. Fourier analyses have yielded the exact values of the exponents,

namely $\alpha = (3-d)/2$ and $\beta = (3-d)/4$ [14]. Arriving atoms maximize their coordination numbers and the surface approaches complete relaxation. When all but v_1 are zero, analysis shows that the exponents α and β are $(5-d)/8$ and $(5-d)/2$, respectively [18]. In this case, the arriving atoms can move to maximize their in-plane coordination number, which leads to an incomplete relaxation of the surface. The case that both η and λ are not zero is generally known as the KPZ equation [15]. Renormalization group (RG) analysis was used to find that the exponents α and β are $1/3$ and $1/2$, respectively, for $1+1$ dimensions. The KPZ non-linear term $(\nabla h)^2$ does not appear for a current-conserving process (no evaporation and vacancies), and the other non-linear term in Eq. (2) was suggested to be relevant for molecular beam epitaxy (MBE) growth processes [18]. An equation keeping only two terms ($\lambda_1, v_1 \neq 0$) was proposed to describe MBE processes, and the RG analysis shows that the exponents α and β are $(5-d)/3$ and $(5-d)/(7+d)$, respectively [18].

2.2. Review of specular X-ray reflectivity

The specular condition implies that the plane containing the incident and reflected X-ray beams is perpendicular to the sample surface, and the incident angle (θ) equals the reflected angle. Specular XR measurements are made by monitoring changes in the reflected X-ray intensity as a function of perpendicular momentum transfer ($Q = 4\pi \sin \theta / \lambda = 2K \sin \theta$). In this way, changes in electron density across interface(s), the thickness of thin films or multilayers and interfacial roughness (width) can be determined. For gold sputter-deposited onto a polished silicon substrate, XR was used to determine the gold electron density, the gold thickness, and the widths of the silicon/gold interface and the gold surface.

X-rays incident on a flat interface, where the electron density abruptly changes, will reflect X-rays according to Fresnel reflectivity [8,21]. Real interfaces, however, are rough on length scales comparable to the X-ray wavelength and do not reflect as well as flat interfaces. Therefore, the reflected amplitude from a real interface is less than that predicted by Fresnel reflectivity for an ideal interface. Generally, this effect becomes more significant with

increasing Q , and a measure of interfacial roughness may be thought of as the amount by which the observed reflectivity differs from the reflectivity of a flat interface. Accordingly, the XR from a rough interface at time t may be written as [8]

$$V^F \int \mathcal{P}(h, t) e^{iQh} dh = V^F P(Q, t), \quad (4)$$

where V^F denotes Fresnel reflectivity, h is a height in the direction normal to the surface, $\mathcal{P}(h, t)$ is a real-space probability distribution function about the average height, $P(Q, t)$ is the momentum space distribution function, and Q is the geometric mean of momentum transfers for two media (i.e. $Q = \sqrt{Q_A Q_B}$ [23,24]). The integration is performed over the height variation of the interface within the X-ray coherence length. A Debye–Waller like damping is typically used for $P(Q, t)$ [21], and $V = V^F e^{-Q^2 \sigma^2 / 2}$, where $\sigma(t)$ is the time-dependent width of the distribution. This is accurate for Gaussian interface fluctuations in the large- Q limit. However, more general non-Gaussian functions have been considered and found to be applicable for several types of interfaces [8,22].

The reflected intensity results from interference between the reflected amplitude from the vacuum/gold interface and the reflected amplitude from the gold/silicon interface. The interference is due to the path difference between the incident and reflected beams. Let the reflection amplitudes from the vacuum/gold interface and from the gold/silicon interface be defined as V_1 and V_2 , respectively. In addition, we define the transmission amplitude from vacuum to gold and gold to vacuum as T_{01} and T_{10} , respectively. Then the reflection intensity becomes

$$I(Q_{\text{vac}}) = \left| V_1 + \frac{V_2 e^{iQ_1 T_{01} T_{10}}}{1 - V_1 V_2 e^{iQ_1 T_{01} T_{10}}} \right|^2 \quad (5)$$

$$V_1 = V^F P(\sqrt{Q_{\text{vac}} Q_{\text{Au}}}, t), \quad (6)$$

$$V_2 = V^F P(\sqrt{Q_{\text{Au}} Q_{\text{Si}}}, t). \quad (7)$$

For our experimental conditions the sputter-deposition rate was constant (0.5 \AA s^{-1}). Therefore, it is convenient for us to define the time of deposition t in units of \AA .

X-rays emitted from a synchrotron source and

subsequently diffracted from a monochromator may be thought of as a collection of photons whose characteristics (e.g. energies, momenta, and polarizations) have a statistical distribution. Each photon behaves as a wave packet when the interference shown in Eq. (5) occurs. The wave packet is composed of a set of momentum components and also has a finite size, according to the uncertainty principle. Therefore, the V s should be evaluated by an integration within the finite dimension of the coherence (coherent average). The coherent average is purely due to the intrinsic nature of the source and upstream X-ray optics. A crude estimation of the coherence volume (the size of the wave packet) for our experimental geometry is an oblate of approximately $6000 \text{ \AA} \times 6000 \text{ \AA} \times 2500 \text{ \AA}$ in size [10], with the smallest axis being perpendicular to the beam and approximately parallel to the surface. For simplicity, we assume that the coherence volume is isotropic to 5000 \AA in radius. Once the coherent average is done for a single photon wave packet, it should be statistically averaged again for many photons (incoherent average). If the photons have different directions relative to the sample due to the beam divergence, or if different parts of the sample have different average characteristics such as thickness of the film, the incoherent average becomes necessary to describe XR correctly. In the case of two interfaces, the inhomogeneity of the thickness and interface width renormalize the thickness and interface width within the coherent average [8], which makes the incoherent average unnecessary. However, the misorientation of the surface and the beam divergence should be considered for incoherent average over a Gaussian distribution of $Q = 0$ for small incident angles after the evaluation of $|\dots|^2$ in Eq. (5) as

$$\langle I(Q_{\text{vac}}) \rangle_{\text{ave}} = \left\langle \left| V_1^F P(\sqrt{Q_{\text{vac}} Q_{\text{Au}}}, t) + \frac{V_2^F P(\sqrt{Q_{\text{Au}} Q_{\text{Si}}}, t) e^{iQ_t T_{01}} T_{10}}{1 - V_1^F P(\sqrt{Q_{\text{vac}} Q_{\text{Au}}}, t) \times V_2^F P(\sqrt{Q_{\text{Au}} Q_{\text{Si}}}, t) e^{iQ_t T_{10}}} \right|^2 \right\rangle_{\text{ave}}, \quad (8)$$

where

$$Q_{\text{Au, Si}} = \sqrt{Q_{\text{vac}}^2 - B_{\text{Au, Si}} F_{\text{Au, Si}}(Q_{\text{vac}}, \omega)},$$

$$B_{\text{Au, Si}} = (9.25, 7.81) \times 10^{-5} \text{ \AA}^{-2},$$

$$V_{1,2}^F = \frac{Q_{\text{vac, Au}} - Q_{\text{Au, Si}}}{Q_{\text{vac, Au}} + Q_{\text{Au, Si}}},$$

and

$$T_{01,10} = \frac{2Q_{\text{vac, Au}}}{Q_{\text{vac}} + Q_{\text{Au}}}.$$

We will refer to $P(\sqrt{Q_{\text{Au}} Q_{\text{Si}}}, t)$ and $P(\sqrt{Q_{\text{vac}} Q_{\text{Au}}}, t)$ as $P(Q, t)$ for simplicity.

Our discussion of $P(Q, t)$ is limited to $2 + 1$ dimensions, which is relevant to our experiments. The destructive interference between X-rays reflecting from different positions on the surface can be written in terms of a surface integral over the surface area (πD^2) [25]

$$P(Q, t) = \frac{1}{\pi D^2} \int_S d\mathbf{x} e^{iQ(h(\mathbf{x}, t) - t)} \quad (9)$$

$$P\{Q, t\} = \frac{\{\Sigma(t)\}^{2/x}}{D'^2} \left[\frac{1}{\alpha y^{2/x}} \gamma\left(\frac{1}{\alpha}, y^2\right) \right] + \left\{ 1 - \frac{\{\Sigma(t)\}^{2/x}}{D'^2} \right\} e^{-y^2}, \quad (10)$$

where $\Sigma(t) = W(\infty, t)$, $y = (1/\sqrt{2})Q\Sigma(t)$, and $D' = D(A/\sqrt{2})^{1/x}$. The time-dependent interfacial width $\Sigma(t)$ is the parameter of interest for the scaling behavior, and the parameter D is the X-ray coherence length, $\sim 5000 \text{ \AA}$ in our experiments.

3. Experimental details

The X-ray reflectivity measurements were performed in situ using a high-vacuum chamber equipped with a faced-magnetron sputtering system and X-ray transparent windows. Details of the chamber and the sputtering geometry are presented elsewhere [27], and only a brief account will be given here. Axial magnetic and radial electric fields ionize Ar gas and accelerate the positive Ar ions at the targets with sufficient energy (200–450 eV) to remove (sputter) neutral gold

atoms. The sputtered gold atoms form a homogeneous “cloud” and deposit onto the substrate. The substrate is located at right angles to the two faced targets, which were kept approximately 5 cm apart, and positioned to remain well below the edge of the plasma. The gold targets were 0.8 mm thick and 25 mm in diameter. The base pressure of the chamber was approximately 1×10^{-5} Torr. Research-grade Ar gas was used for sputtering; gas flow was controlled by a needle valve and 50 l s^{-1} turbomolecular pump. The Ar gas pressure was held at either 1 or 10 mTorr during deposition, as measured by a convection pressure gauge. A low-current (0–20 mA), variable-voltage (0–3000 V) power supply was used to power the faced magnetron sputtering gun and was interfaced to a personal computer. The gun was operated at 300–450 V and the gold deposition rate was $0.5\text{--}1 \text{ Å s}^{-1}$ as determined from XR measurements.

The polished silicon substrates ($1.3 \text{ cm} \times 1.3 \text{ cm} \times 0.15 \text{ cm}$) were cleaned ultrasonically for 5 min each in research grade acetone, ethanol, and distilled water. The substrates were blown dry using nitrogen gas and mounted onto a heating or cooling stage using highly conductive silver cement. Resistive heating was used to heat the sample above room temperature, and a flow-through liquid nitrogen scheme was used to cool to 220 K. The sample temperature was stabilized to better than $\pm 0.5 \text{ K}$.

The X-ray measurements were performed at the National Synchrotron Light Source on beamline X22B. The incident beam was focused in the horizontal and vertical directions by a toroidal nickel-coated aluminium mirror. The incident-beam spot size was $\sim 2 \text{ mm}$ horizontal by $\sim 1 \text{ mm}$ vertical. A single flat Ge(111) crystal monochromator was used, and the incident X-ray wavelength was 1.50 Å . The measurements were performed in the horizontal scattering geometry, and the instrumental resolution was approximately $1 \times 10^{-3} \text{ Å}^{-1}$. The chamber was mounted onto the phi circle of a four-circle diffractometer, and scintillation detectors were used to monitor the incident and reflected X-ray beam intensities. While XR data were being recorded, the power supplied to the faced-magnetron gun was reduced such that the amount of gold deposited during data acquisition was negligible.

At the same time, the plasma was kept active throughout the measurement. A gold “buffer layer” between 50 and 75 Å thick was deposited at $T = 300 \text{ K}$ and $P_{\text{Ar}} = 10 \text{ mTorr}$ before sputtering gold at the desired deposition conditions. Series of XR scans were measured during deposition at $P_{\text{Ar}} = 1$ and 10 mTorr and $T = 220, 300$ and 350 K . The Ar sputtering pressures were chosen such that gold particles incident on the silicon substrate were either (i) thermalized by collisions before deposition onto the silicon surface (10 mTorr) or (ii) had large incident momenta and followed straight-line trajectories before depositing onto the silicon surface (1 mTorr). The substrate temperatures were chosen to investigate the possible effects of surface diffusion.

4. Results and discussion

4.1. Scaling behavior

The specular XR data measured during the deposition of gold on silicon are shown in Fig. 1. Each XR series is plotted with respect to perpendicular momentum transfer and deposition time. The relevant deposition parameters were substrate temperature ($T = 220\text{--}350 \text{ K}$) and Ar gas sputtering pressure ($P_{\text{Ar}} = 1$ or 10 mTorr). The background was determined by performing XR scans in an off-specular condition, i.e. $\theta = (2\theta/2) \pm 0.2^\circ$ (at the specular condition $\theta = 2\theta/2$). This background scan was done only at the end of each series of scans. Since the background increases as the film thickness increases, the measured background at the end of a series is an overestimation for most of the previous scans. However, the background is nearly negligible for most early scans, and should become closer to the estimated background as the deposition progresses. We find that the background subtraction becomes significant only for the last few scans. Therefore, the estimation of background only from the last scan is a fairly good approximation to measuring the background point by point and scan by scan. In short, our means of background subtraction does not affect the fitting of the data or the conclusions drawn from the fit parameters in the following discussions. Geometric

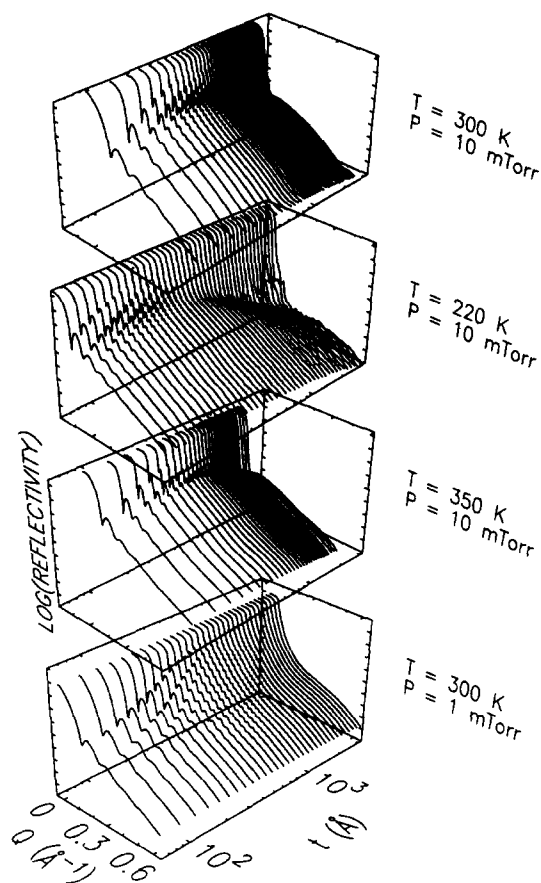


Fig. 1. Specular X-ray reflectivity (logarithmic scale) is plotted against perpendicular momentum transfer (Q) and deposition time (logarithmic scale). The unit of the time axis is in Å (1 Å deposition per approximately 2 s).

effects concerning the amount of the sample surface which was illuminated were corrected by integrating the incident-beam profile.

Profilometry measurements were performed to determine whether the deposition was uniform over the entire substrate surface. The measurements were performed in air after deposition was completed. Within the sensitivity of the profilometer (± 30 Å), the film thicknesses were uniform over the macroscopic extent ($1.3 \text{ cm} \times 1.3 \text{ cm}$) of the sample. From the profilometry results, it is clear that the films grown in our sputtering chamber were homogeneous over the entire sample.

Oscillations in the XR arise from interference effects between the silicon/gold and gold/vacuum

interfaces. The oscillation period is inversely proportional to the gold thickness. As shown in Fig. 1, the oscillation period decreases as the deposition time increases. As the gold thickness increased beyond approximately 1300 Å, the oscillations were no longer resolvable due to a combination of instrumental resolution, absorption of X-rays through the gold, and the relatively large roughness of the gold/vacuum interface. When the thickness of gold and the roughness of the gold/vacuum interface become so large that the absorption of X-rays through gold becomes severe, the interference disappears. In this case, the reflection from the gold/vacuum interface is strong for small Q values but decreases rapidly with increasing Q due to interface roughness. The reflection from the gold/silicon interface is very weak for small Q values (small angles and long path length through gold) due to the absorption. This reflection becomes significant at large Q values (large angles and short path length through gold) because the gold/silicon interface is sharp and remains unchanged throughout the deposition. Therefore, XR at low Q values is mainly from the gold/vacuum interface, and XR at high Q values is mainly from the gold/silicon interface. In the region where the oscillations are discernible, the gold film thickness can be determined accurately from the oscillation period. For thick films, the thickness can be determined fairly accurately from the absorption of the scattering from the gold/silicon interface by the gold layer.

One of the key factors in determining accurately the width of the gold/vacuum interface is the cleanliness of the silicon surface. Even a small amount of fractional surface contamination can lead to changes in the gold density at the interface and can strongly modulate or affect the reflectivity. To ensure that the silicon surface was free of contamination, the surface was baked before the deposition of gold. Fig. 2 shows the XR of a typical silicon surface measured in vacuum (10^{-5} Torr) at $T = 300$ K before gold deposition. The XR was recorded before and after baking the silicon at 500 K. The background was subtracted from the measured XR and the aforementioned geometric correction was also applied. The modulation in the XR indicates the presence of a second interface

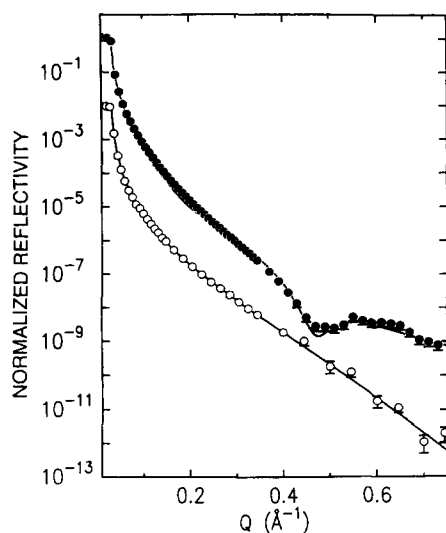


Fig. 2. The X-ray reflectivity of a typical silicon substrate is plotted before (filled circles) and after (open circles) heating to 500 K in vacuum. The solid lines are the best fits to the data as described in the text. The open circles were offset for clarity.

other than the silicon/vacuum interface, probably due to the presence of a hydrocarbon-like layer adsorbed onto the silicon surface. An equation similar to Eq. (8) was used in the modeling of all the XRs presented here. The best fit was obtained using a simple Gaussian distribution to describe the interfacial roughness. The best-fit parameters were: the silicon surface roughness, 3.1 Å; the adsorbed layer thickness, 19.4 Å; and the adsorbed layer electron density, $0.55 \text{ e}^- \text{ Å}^{-3}$. This electron density is roughly equivalent to that of water. The fraction of the second interface for the XR data recorded after bake-out to 500 K was fitted to zero, indicating that a single interface (silicon/vacuum) model is sufficient and the hydrocarbon-like layer is removed from the surface. The density of silicon oxide is known to be very close to that of silicon. Fig. 2 confirms this and also shows that the silicon oxide is compact without voids.

The fits of Eq. (8) to the data shown in Fig. 1 were done in steps. First, several parameters were varied during fitting, including density of gold, X-ray coherence length, instrumental resolution, gold/silicon interfacial width, gold thickness, and the gold/vacuum interfacial width $\Sigma(t)$. By doing so, we can determine whether any fit parameters

change significantly from scan to scan. In addition, estimations based on our experimental geometry of certain parameters can be compared to the fit results. We found that the density of gold (normalized to bulk gold value) is 1.00 or close to 1.00 for the entire deposition range. The fit value of the X-ray coherence length D' was $5.5(5) \times 10^3 \text{ Å}$. The width of the gold/silicon interface was $3.0(5) \text{ Å}$ and remains unchanged over the entire fit range. In the next step, all the fit parameters are fixed to the optimum values determined for all scans in a series, and only \bar{h} and $\Sigma(t)$ were varied. The fit values for \bar{h} and $\Sigma(t)$ were similar to the previous fit values determined in the first step, but with improved precision. In the final step, \bar{h} was fixed to its optimum value for each scan and only $\Sigma(t)$ was varied.

In our study, the exponent α was determined from fitting the XR data and from STM images. The exponent α was not a fit parameter because of the complexity of the analytic form of the incomplete gamma function in our fitting program. Therefore, $\alpha = 1/3$, $2/5$ and $1/2$ were tried, and $2/5$ was found to produce the best fit for the 3500 Å thick film [10].

The second method of determining α was from STM images. The STM image for the high-pressure sample is shown in Fig. 3a, and that for the low-pressure sample in Fig. 3b. The experimental aspects of our STM measurements were discussed in previous publications [10,28]. The $\sqrt{G(x, t)}$ s calculated from the STM images are shown in Fig. 4. The fit value of α (see Ref. [10] for a discussion) was 0.40(2), consistent with the value obtained from the XR scans. On the other hand, the low-pressure data neither shows any obvious scaling behavior nor does the saturation at large x . The comparison will be discussed in Section 4.2.

In Fig. 7, the gold/vacuum interfacial width $\Sigma(t)$ at $P_{\text{Ar}} = 10 \text{ mTorr}$ (circles) and at $P_{\text{Ar}} = 1 \text{ mTorr}$ (squares) is plotted as a function of deposition time. The circles (10 mTorr data) clearly exhibit scaling behavior with growth time. The exponent β was 0.42(2) for the 220 K data (open circles) and 0.40(2) for the 300 K data (filled circles), which falls between $\beta = 1/2$ for the random deposition and $\beta = 1/4$ based on a RSOS model [16] (see Ref. [10] for a more detailed discussion).

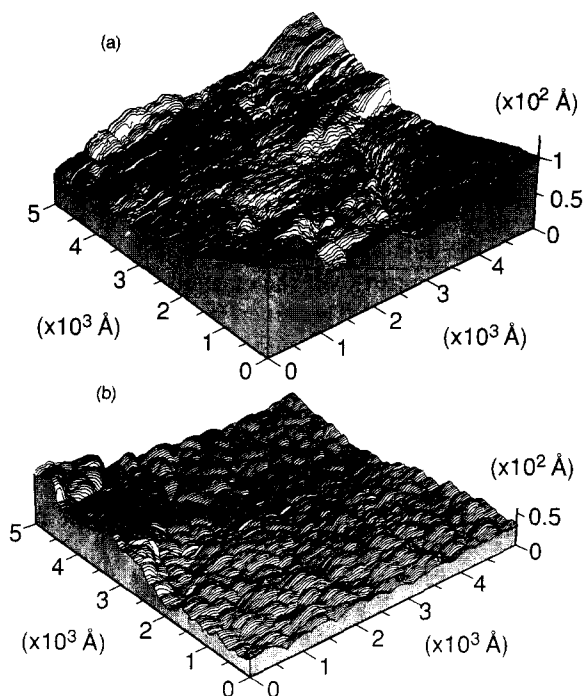


Fig. 3. The STM images of the gold surface after deposition was completed for (a) $P_{Ar} = 10$ mTorr, $T = 220$ K and (b) $P_{Ar} = 1$ mTorr, $T = 300$ K. The samples are the same from which the XR scans shown in Figs. 5 and 6 were taken.

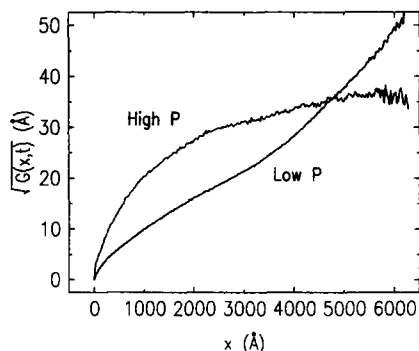


Fig. 4. The height–height distribution function calculated from the STM images shown in Fig. 3.

In earlier work by one of us [29], off-specular X-ray reflectivity measurements were used to determine the self-affine fractal scaling behavior of Ag vapor-deposited onto quartz at 80 K. The temporal behavior of the dynamic scaling exponent β was not determined. However, the roughness exponent

determined by Chiarello et al. ($\alpha = 0.46$ [29]) is in good agreement with the results presented here.

There have also been recent STM studies of the kinetic roughening of gold vapor-deposited onto glass substrates [30]. In this work, gold is believed to form in columnar shapes and two values for the scaling exponents are reported, which depend on the resolution of the STM. In region II, which is sensitive to column-height fluctuations, the authors report $\alpha = 0.37$ and $\beta = 0.45$, which are consistent with our results.

Specular X-ray reflectivity measurements have also been performed for silver vapor-deposited onto polished quartz at approximately 300 K [31]. In this study, the exponents α and β were 0.70 and 0.26, respectively. These values do not correspond with those reported here. As reported by Thompson et al. [31], the difference may be attributed to the different deposition conditions or to their different analysis approach.

It is beyond the scope of this work to review all of the experimental work done on kinetic roughening of non-equilibrium-grown metal films. The reader is referred to Krim and Palasantzas [2], who have written an excellent summary of the experimental results and techniques used to study kinetic roughening of thin metal films.

For the low-pressure data ($P_{Ar} = 1$ mTorr), $\Sigma(t)$ is smaller (compared to gold with the same thickness but grown at $P_{Ar} = 10$ mTorr) and the interfacial width does not increase during the initial growth stages (< 400 Å). This is because a 50–60 Å gold buffer layer was predeposited at $P_{Ar} = 10$ mTorr and the initial growth at $P_{Ar} = 1$ mTorr was smoothing the gold buffer-layer surface. However, $\Sigma(t)$ eventually grows with time. With an assumption that the interfacial width for the low-pressure data eventually follows a scaling law, it was fit to an equation, $\Sigma = \sqrt{\Sigma_0^2 + a(t - t_0)^{2\beta}}$. The best fit was obtained with $\beta = 0.5$ and $t_0 = 310$ Å.

4.2. Dependence of films on argon pressure

In sputter-deposition processes, the argon gas pressure affects both the efficiency of deposition and the trajectory of the sputtered atoms (relative to the substrate surface). In our experimental

geometry, deposition was insufficient for $P_{\text{Ar}} \ll 1$ mTorr or for $P_{\text{Ar}} \gg 10$ mTorr. For $P_{\text{Ar}} \ll 1$ mTorr, there may not have been sufficient Ar^+ present for sputtering as explained by Paschen's law [32]. For $P_{\text{Ar}} \gg 10$ mTorr, the ionized argon could have suffered too many collisions before reaching the target and arrived at the target with insufficient kinetic energy for sputtering, or the sputtered particles may have suffered collisions, lost energy, and returned back to the target. The mean free path of a sputtered particle is $l = kT/\sqrt{2}\pi d^2 p$, or about 10 cm for $P_{\text{Ar}} = 1$ mTorr. The low pressure (1 mTorr) was chosen such that a sputtered gold atom reached the silicon substrate surface after relatively few collisions, and the high pressure (10 mTorr) was chosen such that the sputtered gold atoms collided several times with argon atoms before reaching the silicon substrate surface. Therefore, the gold atoms sputtered at high pressure arrived with random directions and with significantly reduced kinetic energies. The gold atoms sputtered at the low pressure arrived with their initial kinetic energies and without changing their direction of travel.

The XR scans were qualitatively different for the low-pressure and high-pressure depositions, as shown in Fig. 5. We compare the second scans from the top, whose thicknesses are nearly identical. The oscillation periods are quite similar. The oscillation amplitude in Fig. 5a is large for small Q but decreases rapidly as Q increases. On the other hand, the oscillation amplitude in Fig. 5b is small for small Q but decreases slowly as Q increases. A qualitative comparison can be made without detailed analyses of the data. When the film is smooth in all length scales, the oscillation amplitude will be large and decrease slowly as Q increases. When the surface is rough in microscopic length scales (comparable to the X-ray wavelength), the oscillation amplitude will decrease rapidly, even if the film is extremely smooth in global scales. When the surface has large length-scale fluctuations (comparable to the X-ray coherence length), on the other hand, an incoherent average becomes necessary. In this case, the decrease in the oscillation amplitude is weakly dependent on Q . This point can be seen clearly by computer simulations of XR with different degrees of incoherent averaging

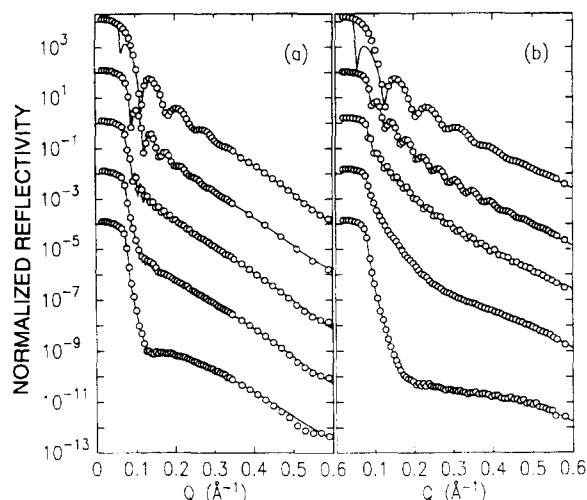


Fig. 5. Examples of the best fits (solid lines) to the X-ray reflectivity data (filled circles) using Eq. (8) of the text. The deposition conditions were $T = 220$ K and $P_{\text{Ar}} = 10$ mTorr for (a) and $T = 300$ K and $P_{\text{Ar}} = 1$ mTorr for (b). The gold film thicknesses were approximately 80, 170, 230, 620, and 2400 Å from top to bottom, respectively. The data were offset for clarity.

ing over the distribution of $Q = 0$. From these qualitative arguments and from the fact that $\Sigma(t)$ is smaller for the low-pressure data, we can conclude, based on the specular reflectivity alone, that the gold surfaces formed at high pressure are microscopically rough but globally smooth, while the gold surfaces formed at low pressure are microscopically smooth but globally rough.

The off-specular scattering of the high-pressure and low-pressure samples is shown in Figs. 6a and 6b, respectively. The directions of H and K were chosen to be perpendicular to the surface (specular) and to the scattering plane (in-plane), respectively. These measurements were made at the completion of the specular XR series. Each off-specular scan was performed by monitoring the scattered X-ray intensity as a function of parallel momentum transfer at a fixed perpendicular momentum transfer. Comparison of Figs. 6a and 6b indicates that there was significant off-specular scattering from the low-pressure film but there was nearly none from the high-pressure film.

Let us compare the off-specular scans with the real-space images shown in Fig. 3. A simple examination shows that the image for the high-pressure

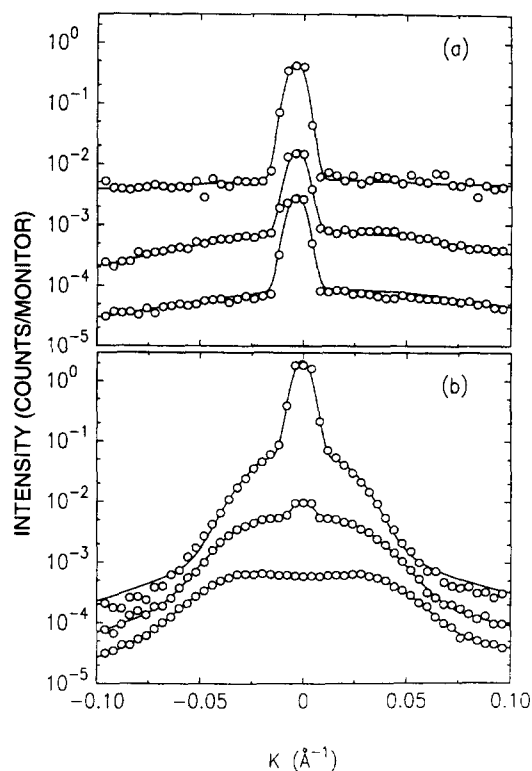


Fig. 6. Transverse (0.1K0), (0.125K0), and (0.15K0) scans from the top, respectively, for gold sputter-deposited onto silicon at $T=220$ K, $P_{Ar}=10$ mTorr (a) and at $T=300$ K, $P_{Ar}=1$ mTorr (b). The scans were recorded in air after gold deposition was completed. The gold thicknesses were 3500 Å for (a) and 3800 Å for (b). The solid lines are guides to the eye.

sample is rough, and the roughness occurs over all length scales. Therefore, the featureless scattering will occur over a wide K range, which is consistent with the off-specular XR data shown Fig. 6a. On the other hand, the image for the low-pressure sample shows structures whose sizes and separation distances are not completely random. The sizes of the bumps and the distances between them are approximately hundreds of Å, which is also consistent with the off-specular scattering at ~ 0.1 Å⁻¹ shown in Fig. 6b.

The distinction between the 10 mTorr and 1 mTorr films can also be seen in the $\sqrt{G(x, t)}$ s of Fig. 4, which were calculated from the STM images. The $\sqrt{G(x, t)}$ for the high-pressure data shows a simple monotonic increase in x , while that for the low-pressure data has an inflection point.

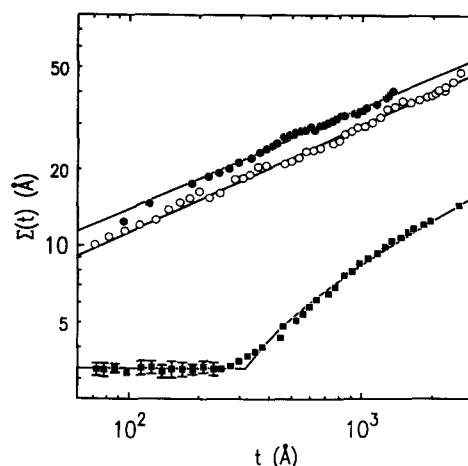


Fig. 7. The width of the gold-vacuum interface is plotted versus gold thickness (log-log scale) under the following deposition conditions: $T=300$ K and $P_{Ar}=10$ mTorr (filled circles), $T=220$ K and $P_{Ar}=10$ mTorr (open circles), and $T=300$ K and $P_{Ar}=1$ mTorr (filled squares). The solid line under the squares (not scaling) is a fit with $\beta=0.5$ and the initial width of 3.2 Å.

For $\sqrt{G(x, t)}$ of the low-pressure data, the relation $G(x, t) = 2\Sigma^2(t)$ is not valid. Instead, Σ should be considered as an average of $\sqrt{G(x, t)}/2$ over the X-ray coherence length. In doing so we can easily see that Σ should be smaller for the low-pressure data than for the high-pressure data. Also notice that $\sqrt{G(x, t)}$ for the low-pressure data continuously increases for $x > 5000$ Å. This clearly supports the above discussion that the surface of the low-pressure sample fluctuates beyond the X-ray coherence length, i.e. the surface is globally rough. A detailed study of off-specular reflectivity from the various length-scale fluctuations, height-difference distribution function from real-space images, and their relations to scaling behaviors, is in progress [34] but is beyond the scope of this paper.

Powder diffraction scans of these samples are shown in Fig. 8. The measurements were made in air using a 12 kW rotating-anode X-ray source (Cu K radiation, $\lambda = 1.54$ Å). The data are plotted as intensity (logarithmic scale) versus 2θ . The positions of the Au(111) and Au(200) Bragg reflections are indicated in the figure. These scans, along with rocking-curve scans, indicate that both samples were textured 2D powders. The low-pressure sample consisted of facets with (111) index

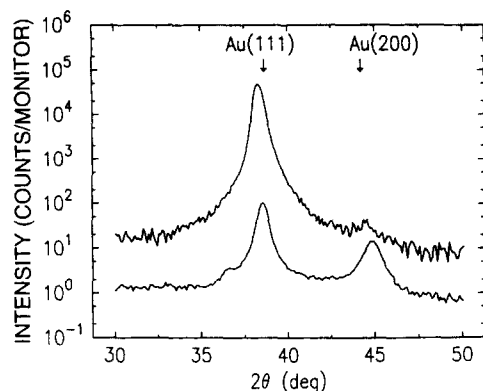


Fig. 8. Powder diffraction scans from gold sputter-deposited onto silicon at (a) $T = 300$ K and $P_{\text{Ar}} = 1$ mTorr and (b) $T = 220$ K and $P_{\text{Ar}} = 10$ mTorr. The scans were recorded in air after gold deposition was completed. The gold thickness was approximately 3500 \AA in both cases. The scans are plotted on a logarithmic scale and one of them is offset for clarity. The expected peak positions for the Au(111) and Au(200) Bragg reflections are indicated by the arrows.

plane faces oriented parallel to the substrate surface. The high-pressure sample consisted of a combination of facets having (111) and (200) faces oriented parallel to the substrate surface plane. The characteristic facet size was approximately 50 \AA . Powder scans from other sputter-deposited gold/silicon samples strongly suggest that a combination of (111) and (200) facets is an effect of P_{Ar} and independent of T over the range 220–350 K.

4.3. Dependence of films on substrate temperature

Selected XR scans measured at $P_{\text{Ar}} = 10$ mTorr and $T = 220$ – 350 K are shown in Fig. 9. The reflectivity scans were normalized by the calculated reflectivity of a semi-infinite flat gold slab. The normalization emphasizes the effect of the gold surface on the measured XR. The amount of gold deposited is nearly identical for each set of three XR scans shown in the Fig. 9. The deposition rates for the 220 and 300 K samples were determined from the XR oscillation frequencies. During the early growth stage ($\leq 230 \text{ \AA}$), the XR appear nearly identical. However, for the thicker films the oscillation amplitudes of the 300 K sample damp faster than those of the 220 K sample. The damping of the oscillation amplitude is related to the inter-

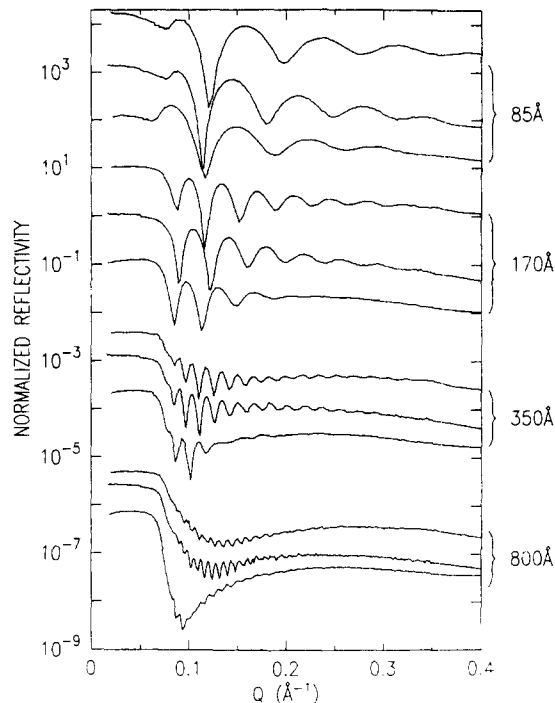


Fig. 9. Normalized reflectivity is plotted as a function of perpendicular momentum transfer illustrating the effect of substrate temperature on reflectivity. The Ar pressure was 10 mTorr. The substrate temperature within each set of scans of indicated thickness are 220, 300 and 350 K.

facial width, and the 300 K sample surface was rougher than the 220 K sample surface for the same film thickness. These differences can be seen quantitatively in Fig. 7.

Initially this result may seem counter-intuitive: one might expect that gold deposited at lower temperature to deposit by ballistic aggregation, and at higher temperature for gold to have greater mobility, resulting in a smoother surface. However, our results are consistent with computer simulation of growth in the restricted solid-on-solid model [33]. In this model, growth at lower temperatures leads to a surface composed of large terraces, because growth occurs mainly at surface defects such as steps and along kinks. At higher temperatures, the surface appears locally rough.

For the substrate temperature of 350 K, the apparent deposition rate (as determined by changes in the XR oscillation frequencies) was considerably smaller than those measured at lower substrate

temperatures. In addition, the oscillation amplitudes were dampened more rapidly (with increasing Q) than those at lower substrate temperatures. The second observation implies that the gold surface becomes rougher more rapidly at higher substrate temperature than at lower substrate temperature. This is evident from the XR scans shown in Fig. 9. Since the sputtering rate from the target and the number of impinging gold atoms should be independent of the substrate temperature, the apparent low deposition rate can be explained by clustering of gold due to sufficient mobility of gold atoms at 350 K. In wetting terminology, the film is in an incomplete wetting situation; therefore, the film and bulk gold coexist. Since the coexisting bulk occupies only a small surface area, the linear relation between the average film thickness and oscillation frequency in XR scans is no longer valid. Since many of the incoming particles go into the bulk gold phase, the film phase of the sample grows at a lower rate.

5. Conclusions

The results presented here indicate that gold films formed by deposition of thermalized gold particles (small incident momenta) are locally rough but globally smooth, while gold films formed by deposition of gold particles with large incident momenta (traveling in straight-line trajectories) are locally smooth but globally rough. Incoherent averaging was not needed to model the $P_{Ar} = 10$ mTorr data, but was required to model the $P_{Ar} = 1$ mTorr data. We also introduce a simple expression to describe X-ray reflectivity from rough interfaces. The model makes use of the dynamic scaling functional form (Eq. (1)) to model interfacial roughness. This model is compared to a simple Gaussian distribution typically used to describe interface roughness. We found that the interfacial width does exhibit scaling behavior for the films grown under high argon pressure. The exponents found in our study for high-pressure data were $\alpha = 0.40$ and $\beta = 0.40(2)$. One of the key features for the dynamic scaling behavior is the fact that α does not change over time. Because of this, the off-specular reflectivity scans measured

during growth should show an identical functional shape for large K . A series of off-specular reflectivity scans showed the expected behavior [34]. Dynamic scaling behavior was not evident for the low-pressure films.

Acknowledgements

This work was supported by the Division of Materials Sciences, Office of Basic Energy Sciences, US Department of Energy, under contract W-31-109-Eng-38. The group at Northwestern University was supported by the National Science Foundation (DMR 8-09854) through the Science and Technology Center for Superconductivity. One of us (H.K.K.) is supported by the Korean Science and Engineering Foundation and RCDAMP.

References

- [1] F. Family, *J. Phys. A* 19 (1986) L441.
- [2] J. Krim and G. Palasantzas, *Int. J. Mod. Phys. B* 9 (1995) 599.
- [3] G.L.M.K.S. Kahanda, X. Zou, R. Farrell and P. Wong, *Phys. Rev. Lett.* 68 (1992) 3741.
- [4] J. Chevrier, V. LeThanh, R. Buys and J. Derrien, *Europhys. Lett.* 16 (1991) 737.
- [5] D. Miller, K.E. Gray, R.T. Kampwirth and J.M. Murduck, *Europhys. Lett.* 19 (1992) 27.
- [6] Y.-L. He, H.-N. Yang, T.-M. Lu and G.-C. Wang, *Phys. Rev. Lett.* 69 (1993) 3770.
- [7] For a review, see I. K. Robinson, in: *Handbook on Synchrotron Radiation*, Vol. III, Eds. D.E. Moncton and G.S. Brown (???).
- [8] H. You, C.A. Melendres, Z. Nagy, V.A. Maroni, W. Yun and R.M. Yonco, *Phys. Rev. B* 45 (1992) 11288.
- [9] R.P. Chiarello, R.A. Wogelius and N.C. Sturchio, *Geochim. Cosmochim. Acta* 57 (1993) 4103.
- [10] H. You, R.P. Chiarello, H.K. Kim and K.G. Vandervoort, *Phys. Rev. Lett.* 70 (1993) 2900.
- [11] M. Eden, *Proceedings of the IV Berkeley Symposium on Mathematics, Statistics and Probability*, Vol. 4, Ed. F. Neyman (University of California Press, Berkeley, 1961) p. 223.
- [12] F. Family and T. Vicsek, *J. Phys. A* 18 (1985) L75.
- [13] M.J. Vold, *J. Colloid Sci.* 14 (1959) 168.
- [14] S.F. Edwards and D.R. Wilkinson, *Proc. R. Soc. London Ser. A* 381 (1982) 17.
- [15] M. Kardar, G. Parisi and Y. Zhang, *Phys. Rev. Lett.* 56 (1986) 889.
- [16] J.M. Kim and J.M. Kosterlitz, *Phys. Rev. Lett.* 62 (1989)

- 2289; J.M. Kim, J.M. Kosterlitz and T. Ala-Nissila, *J. Phys. A: Math. Gen.* 24 (1991) 5569.
- [17] S. Das Sarma and S.V. Ghaisas, *Phys. Rev. Lett.* 69 (1992) 3762.
- [18] Z.-W. Lai and S. Das Sarma, *Phys. Rev. Lett.* 66 (1991) 2348.
- [19] J.D. Jackson, *Classical Electrodynamics* (Wiley, New York, 1975).
- [20] H. You and Z. Nagy, *Current Top. Electrochem.* 2 (1993) ???.
- [21] A. Braslau, P. Pershan, G. Swislow, B.M. Ocko and J. Als-Nielsen, *Phys. Rev. B* 38 (1988) 2457.
- [22] L.B. Lurio, T.A. Rabedeau, P.S. Pershan, I.F. Silvera, M. Deutsch, S.D. Kosowsky and B.M. Ocko, *Phys. Rev. Lett.* 68 (1992) 2628.
- [23] L. Nevot and P. Croce, *Rev. Phys. Appl.* 15 (1980) 761.
- [24] W. Weber and B. Lengeler, *Phys. Rev. B* 46 (1992) 7953.
- [25] S.K. Sinha, E.B. Sirota, S. Garoff and H.B. Stanley, *Phys. Rev. B* 38 (1988) 2297.
- [26] M.V. Berry, *Philos. Trans. Roy. Soc. A* 273 (1973) 611. For clarity, one can rewrite the height–height distribution function in terms of height–height correlation function $C(x)$, as $G(x, t) = 2W^2(x, t)[1 - C(x, t)] = 2\Delta^2(t)[1 - C(x, t)]$.
- [27] J.Q. Zheng, M.C. Shih, X.K. Wang, S. Williams, P. Dutta, R.P. Chang and J.B. Ketterson, *J. Vac. Sci. Technol. A* 9 (1991) 128.
- [28] K.G. Vandervoort, R.K. Zasadzinski, G.G. Galicia and G.W. Crabtree, *Rev. Sci. Instrum.* 64 (1993) ???.
- [29] R.P. Chiarello, V. Panella, J. Krim and C. Thompson, *Phys. Rev. Lett.* 67 (1991) 3408.
- [30] L. Vazquez, R.C. Salvarezza, P. Herrasti, P. Ocon, J.M. Vara and V.J. Arvia, *Surf. Sci.* 345 (1996) 17.
- [31] C. Thompson, G. Palasantzas, Y.P. Feng, S.K. Sinha and J. Krim, *Phys. Rev. B* 49 (1994) 4902.
- [32] F. Paschen, *Wied. Ann.* 37 (1889) 69.
- [33] F. Family, *Physica A* 168 (1990) 561.
- [34] Unpublished.